


Article

Study on Microstructure and Hydrogen Storage Properties of $Mg_{80}Ni_{16-x}Al_xY_4$ ($x = 2, 4, 8$) Alloys

Xia Dong^{1,2}, Yiming Li^{1,2,3,*}, Yutao Zhai⁴, Zhuocheng Liu^{1,3}, Guofang Zhang¹ and Fei Yang^{4,*}

- ¹ School of Materials and Metallurgy, Inner Mongolia University of Science and Technology, Baotou 014010, China; xiad0424@126.com (X.D.); liuzhuo567@126.com (Z.L.); afang1001@126.com (G.Z.)
- ² Key Laboratory of Advanced Metals and Materials of Inner Mongolia, Inner Mongolia University of Science and Technology, Baotou 014010, China
- ³ Collaborative Innovation Center of Integrated Exploitation of Bayan Obo Multi-Metal Resources, Inner Mongolia University of Science and Technology, Baotou 014010, China
- ⁴ Waikato Centre for Advanced Materials and Manufacturing, School of Engineering, University of Waikato, Hamilton 3240, New Zealand; max_zhaiuniv5444@hotmail.com
- * Correspondence: liyiming@imust.edu.cn (Y.L.); fyang@waikato.ac.nz (F.Y.)

Abstract: $Mg_{80}Ni_{16-x}Al_xY_4$ ($x = 2, 4, 8$) alloys were prepared by induction levitation melting, and the effect of substitution of Al for Ni on the microstructure and hydrogen storage properties was studied in the present work. The results illustrated that the solidification path, phase constitution, and grain size were significantly altered by Al addition. Appropriate Al addition improved abundance and grain refinement of the Mg, Mg_2Ni , and $Mg_{15}NiY$ ternary eutectic. But as Al further increased, Mg solidified independently rather than in the formation of the ternary eutectic. More Al favored the formation of Al_3Ni_2Y but suppressed Mg_2Ni and $YMgNi_4$. Although the hydrogen absorption activation and the kinetic property deteriorated, the thermodynamic stability of hydrides was enhanced by adding Al. Hydrogen absorption ability under low pressure was improved, and the $Mg_{80}Ni_8Al_8Y_4$ alloy could absorb nearly 3.5 wt% hydrogen under 1 bar hydrogen at 250 °C.

Keywords: hydrogen storage alloy; Mg-based alloy; grain refinement; low pressure



Citation: Dong, X.; Li, Y.; Zhai, Y.; Liu, Z.; Zhang, G.; Yang, F. Study on Microstructure and Hydrogen Storage Properties of $Mg_{80}Ni_{16-x}Al_xY_4$ ($x = 2, 4, 8$) Alloys. *Metals* **2024**, *14*, 126. <https://doi.org/10.3390/met14010126>

Academic Editor: Andrea Di Schino

Received: 19 December 2023

Revised: 13 January 2024

Accepted: 19 January 2024

Published: 21 January 2024



Copyright: © 2024 by the authors. Licensee MDPI, Basel, Switzerland. This article is an open access article distributed under the terms and conditions of the Creative Commons Attribution (CC BY) license (<https://creativecommons.org/licenses/by/4.0/>).

1. Introduction

Conventional energy sources are gradually proving insufficient to meet contemporary energy demands due to their nonrenewable nature and the associated environmental pollution. Hydrogen energy has emerged as an ideal alternative to conventional sources due to its pollution-free characteristics, abundant availability, and high combustion efficiency. Nevertheless, the practical implementation of hydrogen energy faces persistent challenges related to the development of safe, efficient, and economically viable hydrogen storage methods.

In comparison to high-pressure and liquid hydrogen storage approaches, solid-state hydrogen storage offers considerable advantages in terms of high volumetric hydrogen storage density and enhanced safety, thereby demonstrating significant developmental potential. Among the solid-state hydrogen storage materials, magnesium-based alloys have garnered substantial attention due to their notable attributes, including a high energy density of 7.6 wt% by weight and 110 kg/m³ H₂ by volume, as well as their abundant presence in the Earth's crust [1].

However, the application of Mg-based hydrogen storage alloys remains constrained by the high thermal stability of MgH₂ and the sluggish kinetics of hydrogenation/dehydrogenation processes. Various strategies, including amorphization [2–4], alloying [5,6], nanocrystalline structures [7–11], and catalysis [12–15], have demonstrated efficacy in enhancing the hydrogen storage properties of Mg-based alloys [1,16,17]. Among these strategies, the modification of phase constitution and micro-morphology through the addition of other elements is considered

pivotal for optimizing hydrogen storage properties. During the hydrogenation process, rare-earth magnesium intermetallic compounds, such as REMg_{12} , $\text{RE}_2\text{Mg}_{17}$, and $\text{RE}_5\text{Mg}_{41}$, will decompose into MgH_2 and REH_x nano phases [18]. The nano REHX particles formed through this disproportionation decomposition facilitate nucleation and hydrogen diffusion, thereby effectively enhancing the alloy's hydrogen absorption/desorption kinetics. Due to the positive impact of REH_x phases, the addition of RE elements to magnesium-based alloys has gained widespread acceptance.

In addition to rare-earth (RE) elements, the hydrogen storage properties of Mg-based alloys can be effectively enhanced through the alloying of B-side elements (hydrogen non-affinity elements). The impact of the third transition metals, including Cu, Fe, Co, and Ni, on the hydrogen storage properties of Mg/ MgH_2 has been investigated by Hanada et al. [19], with a particularly positive influence noted for Ni. Yong et al. [20] fabricated $\text{Mg}_{90}\text{RE}_3\text{Ni}_7$ alloy by incorporating Co via mechanical milling. Three distinct hydrogen plateaus were identified, corresponding to $\text{Mg}_6\text{Co}_2\text{H}_{11}/\text{Mg}_2\text{CoH}$, Mg/ MgH_2 , and $\text{Mg}_2\text{Ni}/\text{Mg}_2\text{NiH}_4$, respectively. Improved hydrogen absorption and desorption kinetics were demonstrated, attributed to the preferential nucleation of Mg induced by the chain reaction of $\text{Mg}_6\text{Co}_2\text{H}_{11}/\text{Mg}_2\text{CoH}_5$. Furthermore, Ti and V have been shown to reduce the thermal stability and activation energy of the Mg-Ce-Y-Ni alloys [21]. Overall, introducing secondary metal hydrides through the addition of transition metals can also promote hydrogen diffusion and enhance hydrogen storage properties.

In recent years, Mg-Ni-RE ternary alloys have garnered considerable attention owing to their unique microstructure and hydrogen storage properties. Xie et al. [22] reported that Mg-Ni-Ce alloys demonstrate exceptional kinetic performance, attributed to the catalytic effect of the in-situ formed CeH_3 . Among the Mg-Ni-RE alloys, long-period stacking ordered (LPSO) phases were usually formed in the Mg-Ni-Y alloys. Li et al. found that the 18R-type LPSO phase decomposed under 0.05 MPa hydrogen pressure at 280 °C [23]. Song et al. [24] fabricated an alloy with a composition of $\text{Mg}_{76.87}\text{Ni}_{12.78}\text{Y}_{10.35}$ via induction melting, which included phases such as Mg_2Ni , Mg, Mg_{15}NiY , and MgNi_4Y . The investigation observed that the LPSO phase (Mg_{15}NiY) with a 14H crystal structure undergoes in-situ decomposition into nano RE hydrides during hydrogenation. These nano RE hydrides exhibit a pronounced catalytic effect, thereby enhancing hydrogenation kinetics. The addition of Ce, Ni, and Y effectively introduced multiple reaction pathways and nucleation sites, contributing to a hydrogen pump effect through the transition between $\text{Mg}_2\text{Ni}/\text{Mg}_2\text{NiH}_4$ and YH_2/YH_3 , thereby significantly improving the hydrogenation/dehydrogenation kinetics [25]. Yu et al. prepared $\text{Mg}_{95-x}\text{Ni}_x\text{Y}_5$ ($x = 5, 10, 15$) alloys by vacuum induction melting, among which $\text{Mg}_{80}\text{Ni}_{15}\text{Y}_5$ alloy can absorb hydrogen at 200 °C and presented excellent hydrogen absorption and desorption properties [26].

Alloying with aluminum (Al) has found widespread applications in various hydrogen storage alloy systems, including AB_5 , superlattice A_2B_7 , V-based solid solutions, and Mg-based alloys [27–32]. Notably, Mg-Al intermetallics such as $\text{Mg}_{17}\text{Al}_{12}$ and Mg_2Al_3 have been identified for their capacity to engage in reactions with hydrogen, thereby enhancing the decomposition kinetics of MgH_2 [33–36]. In a study conducted by Lu et al. [37], the dehydrogenation enthalpy was observed to decrease from 77.9 kJ/mol to 70.8 kJ/mol for the $\text{Mg}_{90}\text{Al}_{10}$ alloy compared to pure Mg. Similar results were reported by Zhong et al. [38]. Additionally, the work of Cao et al. [39] highlighted that the introduction of Al into Mg_2Ni resulted in grain refinement and improved thermodynamics (53.9 kJ/mol), attributed to the formation of AlNi .

These studies have highlighted the effectiveness of aluminum (Al) in enhancing the hydrogen storage properties of Mg-based alloys, though a comprehensive investigation is still lacking. While practical applications of Mg-based alloys are currently limited, efforts are underway to explore potential scenarios such as solid-state hydrogen storage [40]. In certain applications, such as hydrogen purification [41], the heightened dehydrogenation temperature no longer serves as the predominant limitation for magnesium-based hydrogen storage alloys. Instead, greater emphasis is placed on discerning hydrogen

absorption characteristics, encompassing parameters such as hydrogen absorption temperature, plateau, and low-pressure hydrogen absorption kinetics. While considerable attention has been directed towards the dehydrogenation thermodynamics and kinetics of Mg-based alloys, hydrogen absorption properties, especially under low-pressure conditions, are frequently overlooked.

Given that dramatic alloying effects can be introduced by Al addition, substitution by Al has seldom been reported in the Mg-Ni-Y system. In the present study, we systematically investigated the effects of aluminum (Al) on the microstructure and hydrogen storage properties of $\text{Mg}_{80}\text{Ni}_{16-x}\text{Al}_x\text{Y}_4$ alloys ($x = 2, 4, 8$). Effort was placed on hydrogen absorption thermodynamics and kinetics under varying temperatures and hydrogen pressures. We paid particular attention to hydrogen absorption ability under a hydrogen pressure of no more than 1 bar.

2. Experiment

2.1. Alloy Preparation

The $\text{Mg}_{80}\text{Ni}_{16-x}\text{Al}_x\text{Y}_4$ ($x = 2, 4, 8$) alloys were prepared by induction levitation melting in a water-cooled copper crucible under an argon atmosphere. The purity of the raw Mg, Y, Ni, and Al elements was greater than 99.5%. Y-Ni binary alloys were first melted three times for homogeneity. Then, Mg and Al metals were added and remelted three times again. Excess Mg (10 wt%), Al (5 wt%), and Y (5 wt%) were added to compensate for the evaporative loss during melting. The three alloys were referred to as Al₂, Al₄, and Al₈ alloys, respectively.

2.2. Characterization

Phase constitution and crystal structure of the as-cast alloys were characterized by X-ray diffraction (XRD, Rigaku-SmartLab, Rigaku, Tokyo, Japan) with Cu K α radiation by a step of 0.02° under 40 kV and 40 mA. For data analysis, Rietveld refinement on XRD datasets was conducted with Maud (Material analysis using diffraction, Maud v.2.33 version, Luca Lutterotti Research Group, University of Trento, Trento, Italy). Firstly, the standard crystal structure (added by CIF files) was imported, and the unit cell parameters were adjusted based on the measured XRD profiles one by one. Then, the background of XRD was refined based on the instrument parameters, including the wavelength of the X-ray, diffraction type (B-B type), the range of tested angles, etc. Next, the proportion factors, peak shape parameters, lattice parameters, atomic position parameters, etc., of each phase were modified. Finally, all the phase structures were added, and the refinement was successively conducted by background, basic phase parameters, microstructure parameters, crystal structure parameters, texture factors, and strain factors. Crystallographic Information Files (CIFs) from the ICSD database were used in the procedure of the Rietveld refinement, as shown in Table S1. The R_{wp} value is the residual calculated directly from the XRD spectrum calculated by the model structure and the experimental data after adding weights to a specific position, which is a description of the fitted graph. The results are generally considered to be credible when the R_{wp} value is <15% [42].

Microstructure morphology was observed by electron probe X-ray micro-analyzer (EPMA, JEOL Ltd., Tokyo, Japan) under backscattered electron mode (BSE). The chemical information was measured by energy dispersive spectroscopy (EDS) equipped on EPMA.

2.3. Hydrogen Storage Property

Heat changes in hydrogenation and dehydrogenation were measured by high-pressure differential scanning calorimetry (HPDSC, NETZSCH-DSC 204 HP, NETZSCH, Selbu, Germany). The hydrogen storage capability and kinetic properties were measured by Setaram-PCTPRO (Hy-Energy, Newark, CA, USA) using Sievert's method [43]. To fully activate, the samples were first pumped at 100 °C for 2 h and then cycled under 3 MPa pressure at 300 °C five times. Each hydrogenation/dehydrogenation cycle consists of absorption at 3 MPa for 1h and desorption by evacuating for 2 h at 300 °C. Pressure-

composition–temperature (PCT) absorption curves were measured at 200 °C, 250 °C, and 300 °C, and the enthalpy changes were calculated based on Vant’ Hoff equation.

3. Experimental Results and Discussion

3.1. Phase Composition of the Original as-Cast Alloys

Presented in Figure 1 is the X-ray diffraction (XRD) pattern of the as-cast $\text{Mg}_{80}\text{Ni}_{16-x}\text{Al}_x\text{Y}_4$ ($x = 2, 4, 8$) alloys. Analysis of the XRD pattern reveals Mg, Mg_2Ni , YMgNi_4 , Mg_{15}NiY , and AlNi phases in the $\text{Mg}_{80}\text{Ni}_{14}\text{Al}_2\text{Y}_4$ alloy. Additionally, minor $\text{Al}_3\text{Ni}_2\text{Y}$ can also be identified through comparison with the XRD curve of the $\text{Mg}_{80}\text{Ni}_8\text{Al}_8\text{Y}_4$ alloy. The standard crystal structures from ICSD (The Inorganic Crystal Structure Database) are listed in Table S1 in the Supplementary Materials. The cell parameters of the phase structures are refined and displayed in Table S2 in the Supplementary Materials. Since the standard structure of LPSO is still unclear, the determination of the unit cell parameters of LPSO was ignored. Unit cells of Mg and Mg_2Ni are larger than the standard crystal structure, which may be caused by a trace of solid solution of Y and Al. The Mg_{15}NiY phase was characterized by TEM, as shown in Figure 2. From electron diffraction and HRTEM analyses, Mg_{15}NiY was identified as a typical 14H-type LPSO [44]. Different from the ternary Mg–Ni–Y alloys, the Al–Ni or Al–Ni–Y phases were introduced by Al substitution. In addition, compared with the similar $\text{Mg}_{80}\text{Ni}_{15}\text{Y}_5$ alloy [26], where the main phases were also Mg and Mg_2Ni , the Y–Ni phase was reported in the ternary alloy.

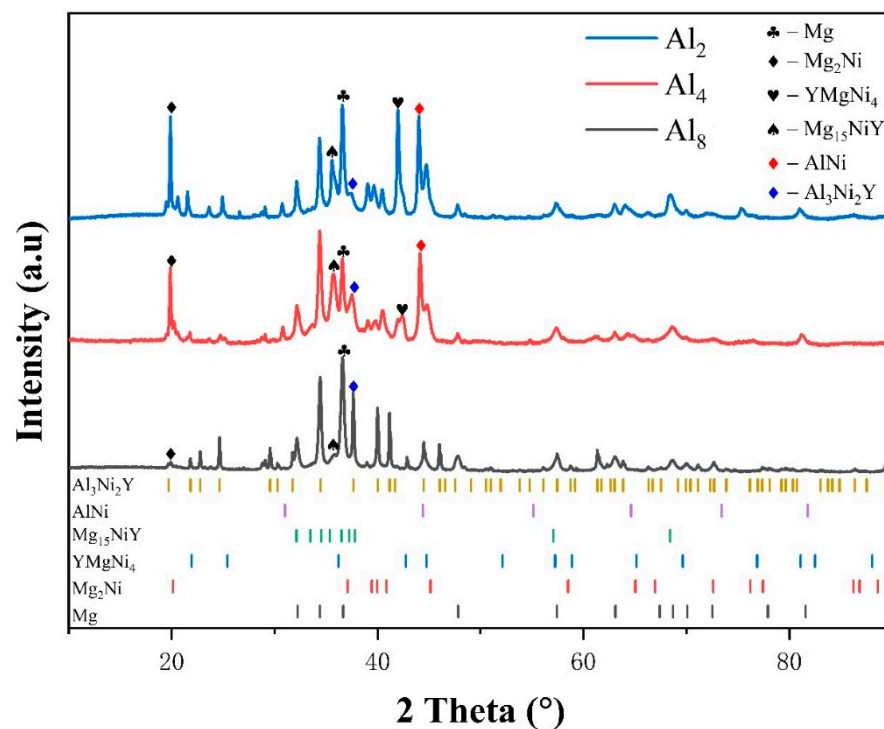


Figure 1. XRD patterns of as-cast $\text{Mg}_{80}\text{Ni}_{16-x}\text{Al}_x\text{Y}_4$ ($x = 2, 4, 8$) alloys.

As Al substitution increases (i.e., the Ni content decreases), there is a notable alteration in the content and type of constituent phases. The phase composition of the $\text{Mg}_{80}\text{Ni}_{12}\text{Al}_4\text{Y}_4$ alloy remains identical to that of the $\text{Mg}_{80}\text{Ni}_{14}\text{Al}_2\text{Y}_4$ alloy. However, with the preferential binding of elemental nickel by aluminum, there is a reduction in the Mg_2Ni phase. In the case of the $\text{Mg}_{80}\text{Ni}_8\text{Al}_8\text{Y}_4$ alloy, there is a substantial emergence of the $\text{Al}_3\text{Ni}_2\text{Y}$ phase. Additionally, this is accompanied by a notable reduction in the Mg_2Ni phase, along with the disappearance of the YMgNi_4 and AlNi phases. All three alloys contain Mg, Mg_2Ni , and Mg_{15}NiY phases, and the contents of the Mg_2Ni and Mg_{15}NiY phases are inversely proportional to the amount of Al substitution. In addition, the cell parameters of Mg and

Mg_2Ni gradually decrease (as indicated in Table S2) as Al increases. This may result from a decrease in Y or Al dissolving due to the consumption of Y-Al compounds.

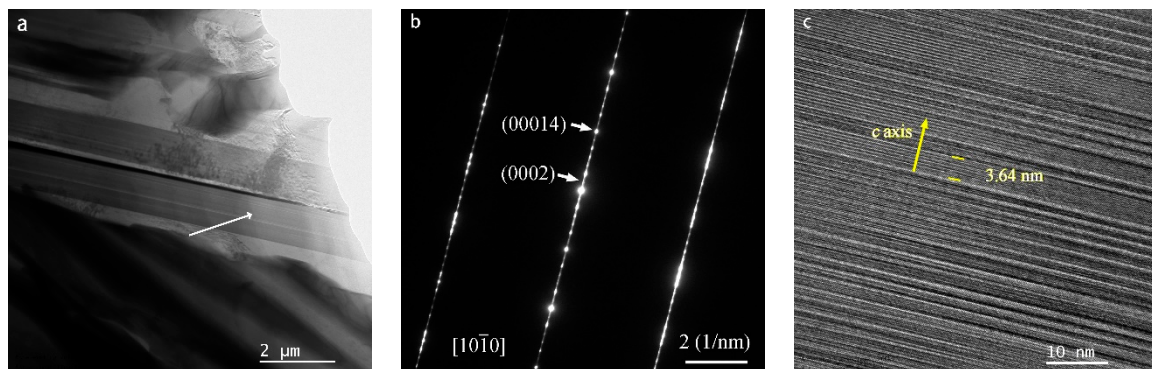


Figure 2. The TEM results of as-cast $Mg_{80}Ni_8Al_8Y_4$ alloy: (a) bright field image; (b) diffraction pattern; and (c) HRTEM of the LPSO $Mg_{15}NiY$.

3.2. Microstructure of the Original as-Cast Alloys

EPMA-BSE images showed five different contrasts in the as-cast $Mg_{80}Ni_{14}Al_2Y_4$ alloy, as displayed in Figure 3. Combined with the EDS results (listed in Table 1), the large block phase presents a bright contrast and is identified as $YMgNi_4$ (marked with “B”), deduced by the quantitative chemical measurement. Moreover, the $AlNi$ phase with relatively bright contrast exhibited a little square shape marked with “C”. Furthermore, the ternary eutectic composed of Mg, Mg_2Ni , and $Mg_{15}NiY$ is illustrated in Figure 3d. Mg presents a black contrast marked with “A”, which is attributed to the low average atomic number. This morphology was also reported in other works on Mg-RE-Ni-based alloys [24,45–48]. It should be noted that large strip shape $Mg_{15}NiY$ can also be observed in the as-cast $Mg_{80}Ni_{14}Al_2Y_4$ alloy, indicating $Mg_{15}NiY$ solidified by both proeutectic and eutectic processes. In addition, Al_3Ni_2Y could not be observed in the EPMA test, possibly due to its low content.

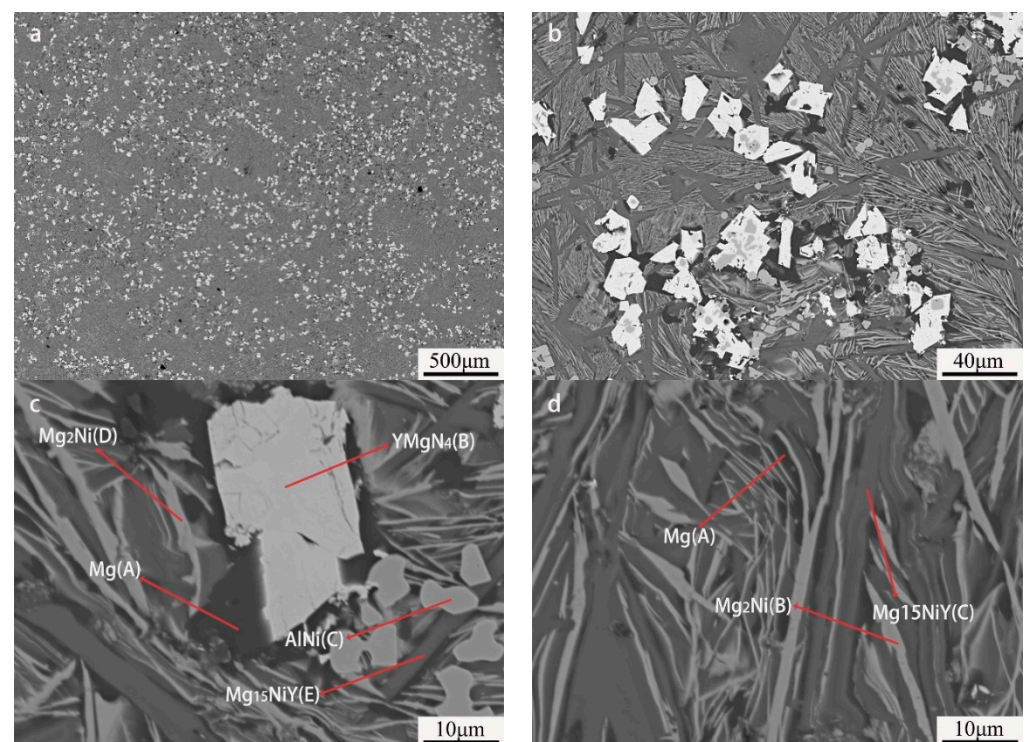
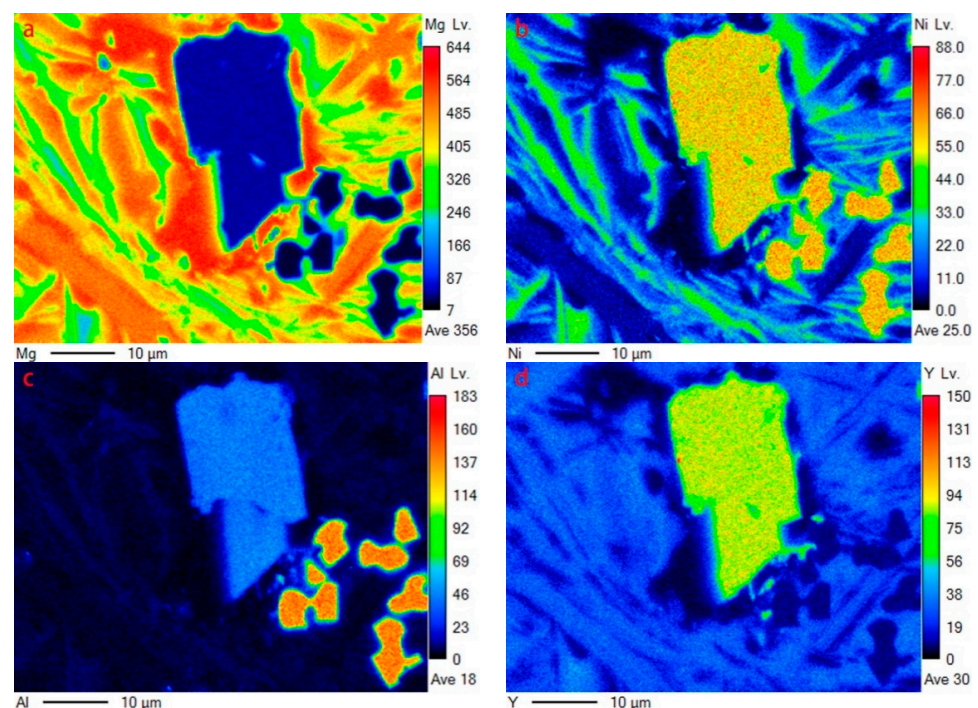


Figure 3. BSE images of $Mg_{80}Ni_{14}Al_2Y_4$ as-cast alloy: (a) 40 \times ; (b) 500 \times ; (c,d) 2000 \times .

Table 1. EDS data of $Mg_{80}Ni_{16-x}Al_xY_4$ ($x = 2, 4, 8$) as-cast alloys.

Alloys	Position	Atomic Percent (%)				Phase
		Mg	Ni	Al	Y	
Al ₂	A	98.42	1.58	-	-	Mg
	B	15.16	63.84	5.41	16.00	YMgNi ₄
	C	-	48.51	51.49	-	AlNi
	D	71.15	25.47	-	3.38	Mg ₂ Ni
	E	94.06	2.85	-	3.09	Mg ₁₅ NiY (LPSO)
Al ₄	A	98.50	1.50	-	-	Mg
	B	-	49.69	51.31	-	AlNi
	C	15.78	59.80	6.54	17.88	YMgNi ₄
	D	91.66	5.22	4.12	-	Mg ₁₅ NiY (LPSO)
	E	73.01	22.63	-	4.36	Mg ₂ Ni
Al ₈	A	99.55	0.45	-	-	Mg
	B	-	33.86	48.03	18.11	Al ₃ Ni ₂ Y
	C	90.14	4.07	-	5.46	Mg ₁₅ NiY (LPSO)
	D	70.23	26.56	-	3.21	Mg ₂ Ni

The same characteristics can be illustrated by EDS mapping (corresponding to the region in Figure 3c), as shown in Figure 4. Y element is mainly dissolved in YMgNi₄ and Mg₁₅Ni (see Figure 4d). Furthermore, Y can be detected in Mg₂Ni, as illustrated by both the EDS quantitative test and mapping characterization, indicating a solid solution of Y in Mg₂Ni, while Y can hardly be detected dissolving in Mg, which is attributed to the low solid solution ability of Y in Mg. In addition, the Al element is mainly distributed in AlNi and YMgNi₄, and little Al can also be observed in Mg₂Ni, as displayed in Figure 4c.

**Figure 4.** EDS mapping of Figure 3c: (a) Mg; (b) Ni; (c) Al; (d) Y.

As to the $Mg_{80}Ni_{12}Al_4Y_4$ alloy, five contrasts can be observed, as shown in Figure 5a,b, which are similar to that of the $Mg_{80}Ni_{14}Al_2Y_4$, based on the chemical composition quantitative analysis. It is obvious that block-shaped YMgNi₄ decreased, and the size became small, as shown in Figure 5b,c, which is consistent with the XRD characterization. Combined with the morphology and EDS mapping observation (see Figure 6), an abundance of the

$Mg_{15}NiY$ phase increased. In addition, the ternary eutectic microstructure tends to be more fine, indicating the grain refinement effect of adding Al. Furthermore, $AlNi$ became coarser and squarer, as illustrated in Figure 5c. The result indicated that increasing Al promoted the development of $AlNi$.

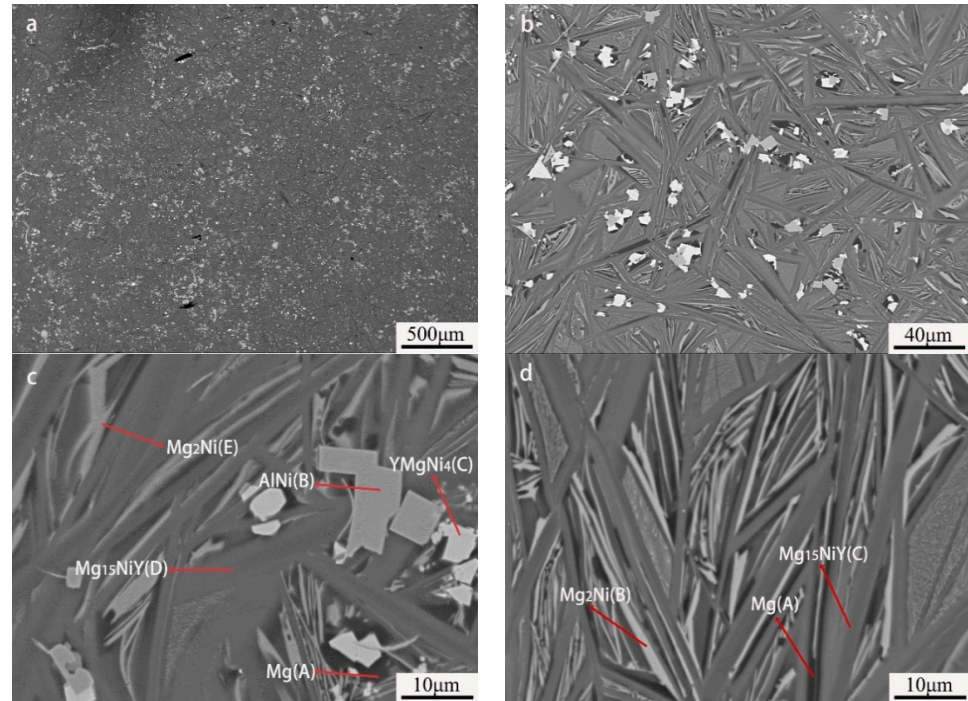


Figure 5. BSE images of $Mg_{80}Ni_{12}Al_4Y_4$ as-cast alloy: (a) 40 \times ; (b) 500 \times ; (c,d) 2000 \times .

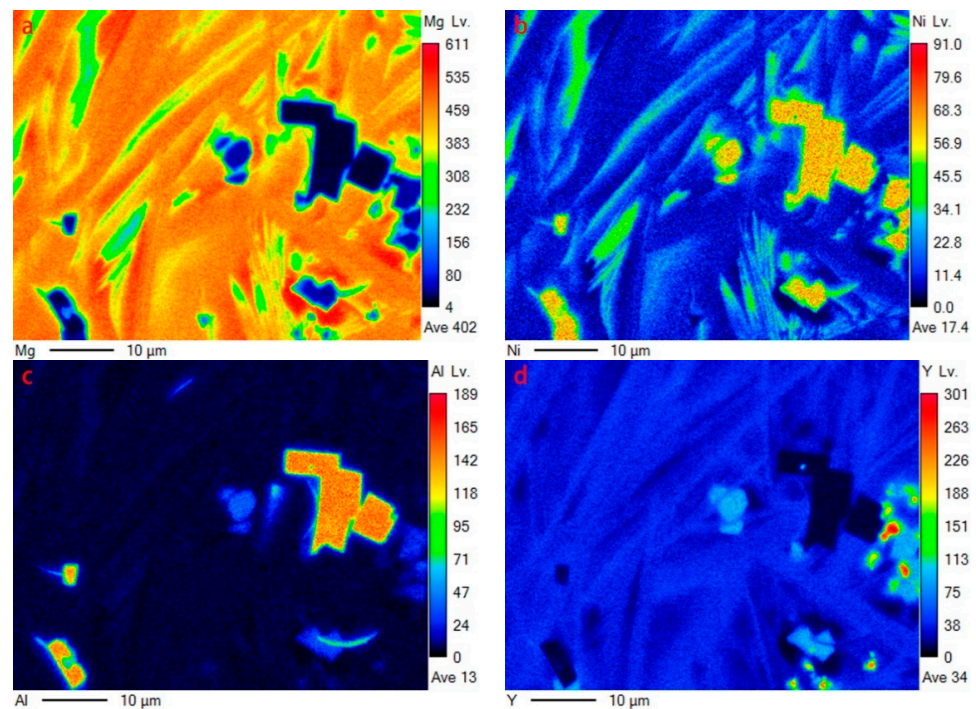


Figure 6. EDS mapping of Figure 5c: (a) Mg; (b) Ni; (c) Al; (d) Y.

By further increasing Al, the microstructure morphology significantly changed, as displayed in Figure 7. A large number of squared phases with bright contrast can be observed in the $Mg_{80}Ni_8Al_8Y_4$ alloy. Chemical composition analysis of the bright phases

confirmed the formation of $\text{Al}_3\text{Ni}_2\text{Y}$ (marked with “B”). Different from the Al_2 and Al_4 alloys, Mg presented block grains instead of strip eutectic morphology. Mg_2Ni and Mg_{15}NiY dramatically decreased according to EDS mapping (Figure 8b,d), which agreed well with the XRD result. This resulted from the great expropriation of Y and Ni by the abundant formation of $\text{Al}_3\text{Ni}_2\text{Y}$. In addition, ternary eutectic microstructure was absent, but Mg_2Ni and Mg_{15}NiY binary eutectic appeared. Obviously, adding more Al led to a change in the solidification routes, where the formation of Mg separated from the ternary eutectic. On the contrary, grain coarsening was caused by adding more Al.

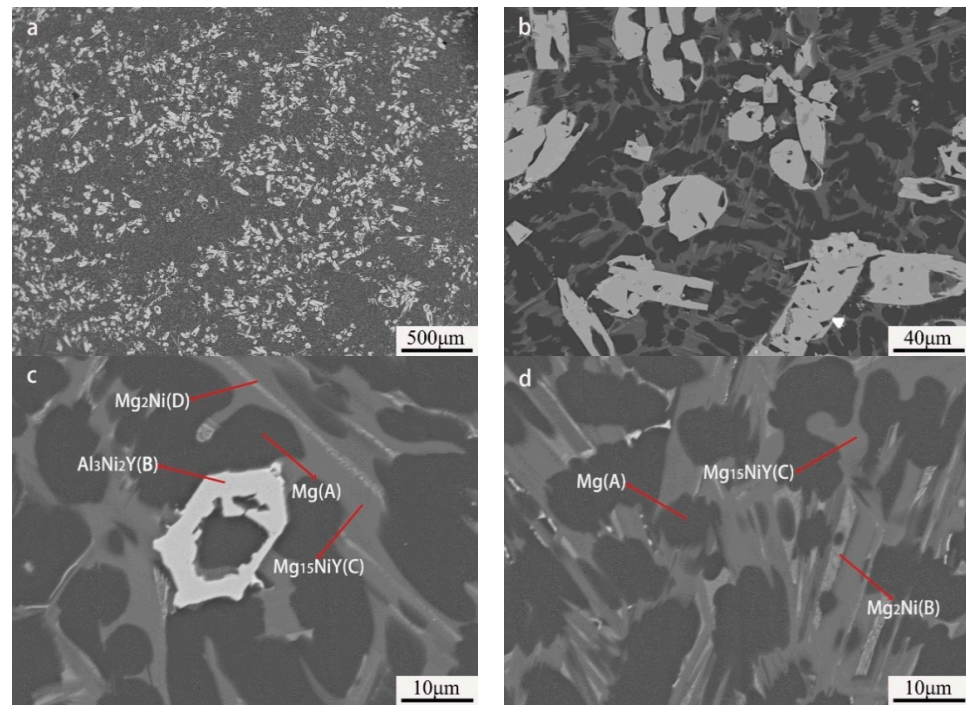


Figure 7. BSE images of $\text{Mg}_{80}\text{Ni}_8\text{Al}_8\text{Y}_4$ as-cast alloy: (a) 40 \times ; (b) 500 \times ; (c,d) 2000 \times .

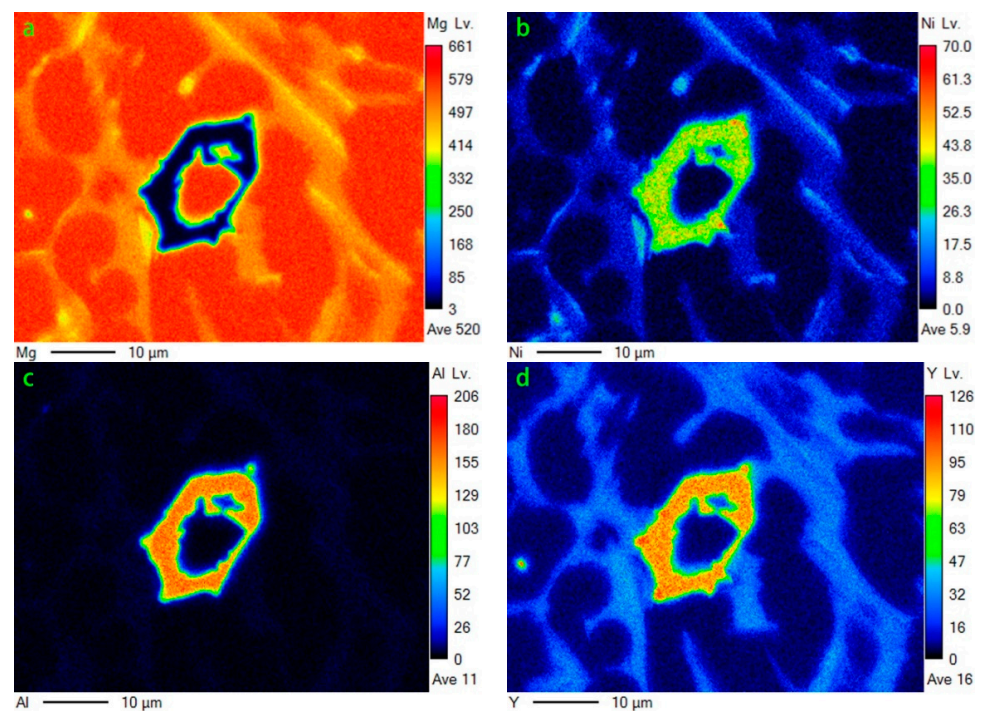


Figure 8. EDS mapping of Figure 7c: (a) Mg; (b) Ni; (c) Al; (d) Y.

3.3. Hydrogen Absorption/Desorption Activation and Kinetic Properties

Figure 9 shows the PDSC curves of the first hydrogenation and dehydrogenation of the three alloys. Al₂ alloy presents an exothermic peak of around 160 °C when heating under hydrogen pressure, which corresponds with the hydrogenation process. A similar exothermic peak can be observed for the Al₄ alloy. However, a delayed exothermic peak around 250 °C occurred for the Al₈ alloy. This may be attributed to the coarse microstructure or dense oxidation coating due to the addition of a lot of Al. The dehydrogenation behaviors of the three alloys exhibit a decreasing trend with decreasing Al content, indicating a negative effect of Al on the activation property.

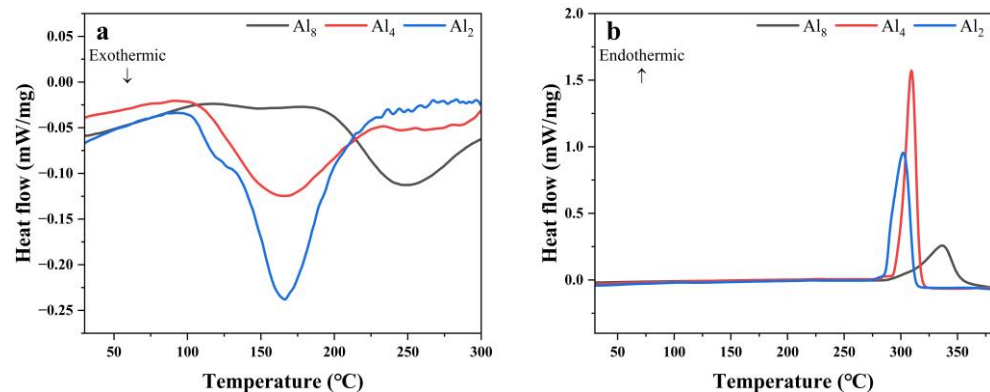


Figure 9. PDSC curves of Mg₈₀Ni_{16-x}Al_xY₄ (x = 2, 4, 8) alloy at 2 °C/min: (a) hydrogen absorption; (b) hydrogen desorption.

Figure 10 illustrates the first hydrogen absorption and isothermal cycling hydrogen absorption curves during the activation process of the as-cast alloy Mg₈₀Ni_{16-x}Al_xY₄ (x = 2, 4, 8). It is evident that the initial hydrogen absorption rate exhibits marked variations. Figure 10a presents the initial hydrogen absorption curves of the three alloys under conditions of 300 °C and 3 MPa hydrogen pressure. Substantial disparities are evident among the initial activation hydrogen absorption curves of the three alloys. Specifically, the Al₂ and Al₄ alloys exhibit no activation period, enabling rapid hydrogen absorption, whereas Mg₈₀Ni₁₂Al₈Y₄ demonstrates a more prolonged activation period. The Al₂, Al₄, and Al₈ alloys exhibit initial hydrogen absorption capacities of 1.97 wt.%, 1.77 wt.%, and 0.29 wt.% within the first 20 min, respectively. It is evident that the initial hydrogen absorption property of the alloys gradually declines with an increase in Al substitution.

Figure 10b,c depicts the cyclic activation hydrogen absorption curves. Friedrichs et al. [49] reported that an unavoidable oxide layer, approximately 3–4 nm thick, forms on the surface of Mg during experimental processes, even when protected by inert gas. During the initial hydrogen absorption stage, hydrogen must traverse the oxide layer before penetrating the alloy's interior, severely impeding hydrogen absorption performance. Following the completion of the initial hydrogen absorption, the oxide layer ruptured, leading to a significant increase in the rate and capacity of subsequent hydrogen absorption. The third hydrogen absorption curve of the Mg₈₀Ni₁₄Al₂Y₄ alloy essentially overlaps with the second curve, indicating completion of activation. In contrast, the Al₄ and Al₈ alloys require four and five hydrogen absorption/desorption cycles, respectively, for full activation. In summary, Mg₈₀Ni₁₄Al₂Y₄ alloy has the best activation properties; Mg₈₀Ni₁₂Al₄Y₄ is the next best, and Mg₈₀Ni₈Al₈Y₄ is the worst.

Figure 11 illustrates the hydrogen absorption curves of fully activated Mg₈₀Ni_{16-x}Al_xY₄ (x = 2, 4, 8) as-cast alloys under a hydrogen pressure of 3 MPa and temperatures of 200, 250, and 300 °C. The results indicate that the hydrogen absorption kinetics curves of the alloys exhibit nearly identical processes, particularly at temperatures of 250 and 300 °C.

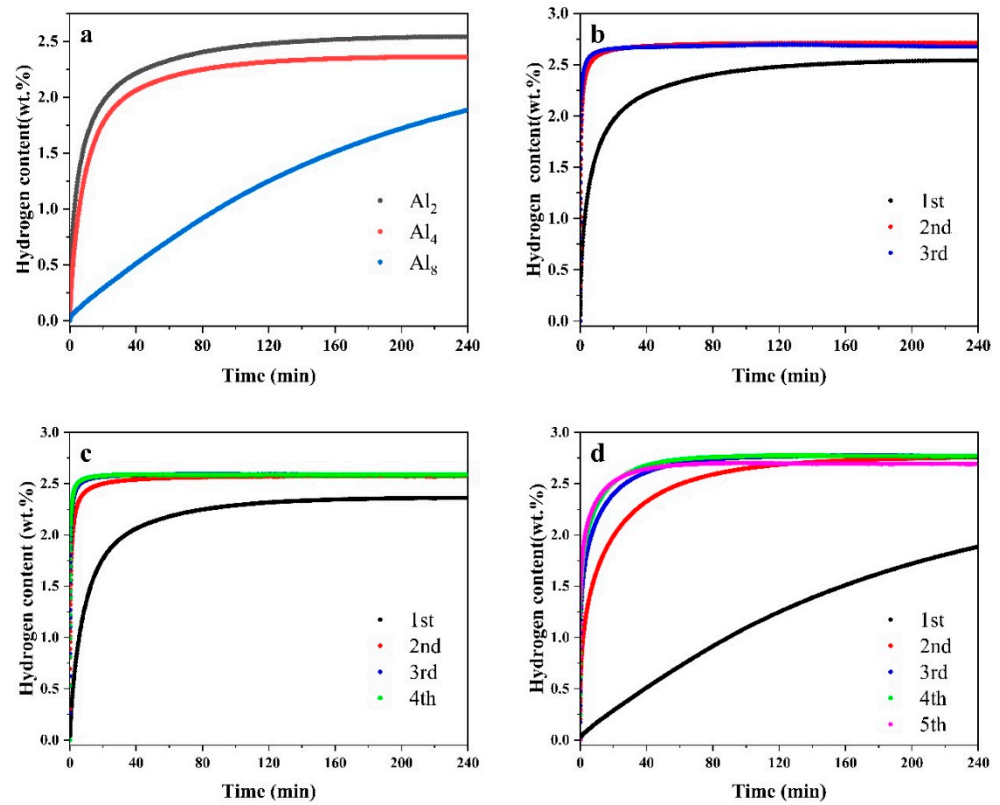


Figure 10. Activation hydrogen absorption curve of $Mg_{80}Ni_{16-x}Al_xY_4$ ($x = 2, 4, 8$) alloy: (a) the first activation of hydrogen absorption and cycles of (b) Al_2 , (c) Al_4 , and (d) Al_8 alloys.

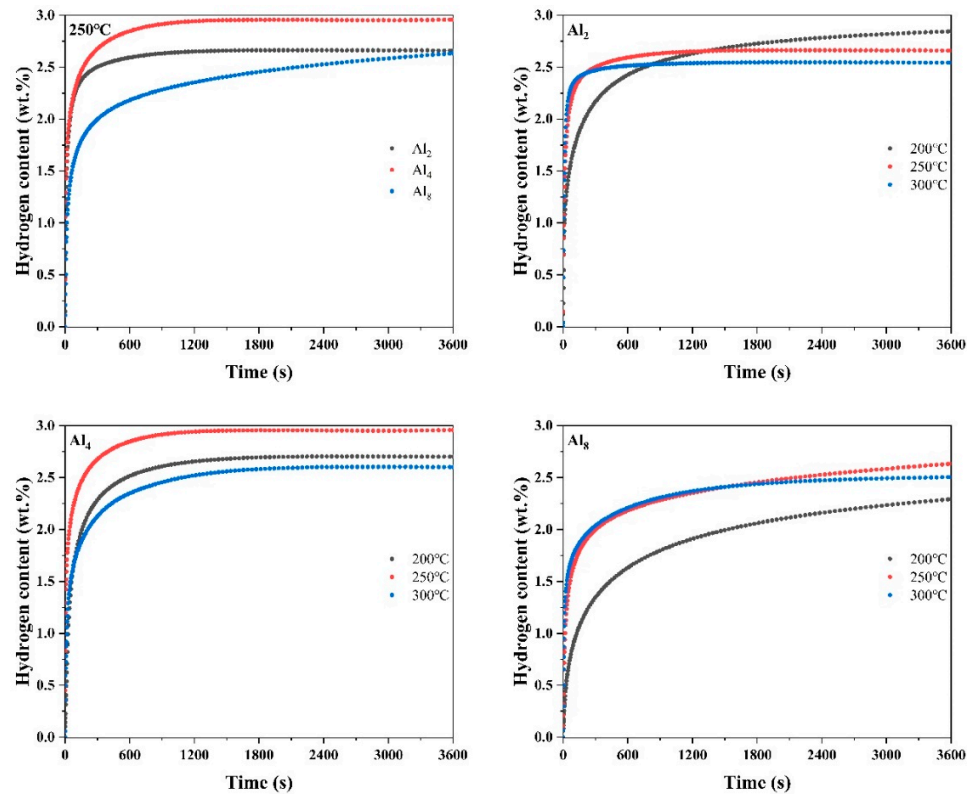


Figure 11. Hydrogen absorption curves of $Mg_{80}Ni_{16-x}Al_xY_4$ ($x = 2, 4, 8$) alloy at different temperatures.

The temperature plays a crucial role in the hydrogen absorption process. Firstly, the absorption is an exothermic process, and a decrease in temperature favors the progression of

the hydrogen absorption reaction. However, the reduction in temperature is accompanied by the suppression of hydrogen diffusion rates, thereby weakening hydrogen absorption kinetics. Therefore, there exists an optimal hydrogen absorption temperature for the absorption process. As depicted in Figure 11, the optimal hydrogen absorption temperature for all three alloys is 250 °C. In Figure 11, at 250 °C, the as-cast alloys of Al₂, Al₄, and Al₈ can absorb 2.66 wt.%, 2.96 wt.%, and 2.63 wt.% H₂ in 3600 s, respectively. The Al₄ alloy exhibits the highest hydrogen-absorbing capacity. However, it is noteworthy that the elevated Al substitution decelerates the hydrogen absorption rate, especially at low temperatures.

To assess the kinetic characters further, the apparent activation energy E_α was calculated based on the Johnson–Mehl–Avrami (JMAK) [50] kinetic model using the Arrhenius equation [51], where T is the hydrogen absorption temperature; R is the gas constant, and A is the frequency factor.

$$\ln[-\ln(1-\alpha)] = \eta \ln k + \eta \ln t \quad (1)$$

where α (0–1) denotes the fraction of Mg converted to MgH₂ at moment t (i.e., hydrogen uptake/maximum hydrogen uptake); k is a kinetic parameter, and η denotes the Avrami index.

$$k = A \exp\left(-\frac{E_\alpha}{RT}\right) \quad (2)$$

Figure 12d shows the Arrhenius plots of Mg₈₀Ni_{16-x}Al_xY₄ ($x = 2, 4, 8$) as-cast alloys; the corresponding data are listed in Table S3 in the Supplementary Materials. The apparent activation energies of hydrogen absorption for Mg₈₀Ni₁₄Al₂Y₄, Mg₈₀Ni₁₂Al₄Y₄, and Mg₈₀Ni₈Al₈Y₄ alloys are 46.36, 48.27, and 59.82 kJ/mol, respectively. The three alloys have significantly lower hydrogen absorption activation energies compared to pure MgH₂ (70.76 kJ/mol) [52]. The apparent activation energies of hydrogen absorption of the alloys are linearly related to the Al content, and Al₂ has the lowest apparent activation energy of hydrogen absorption.

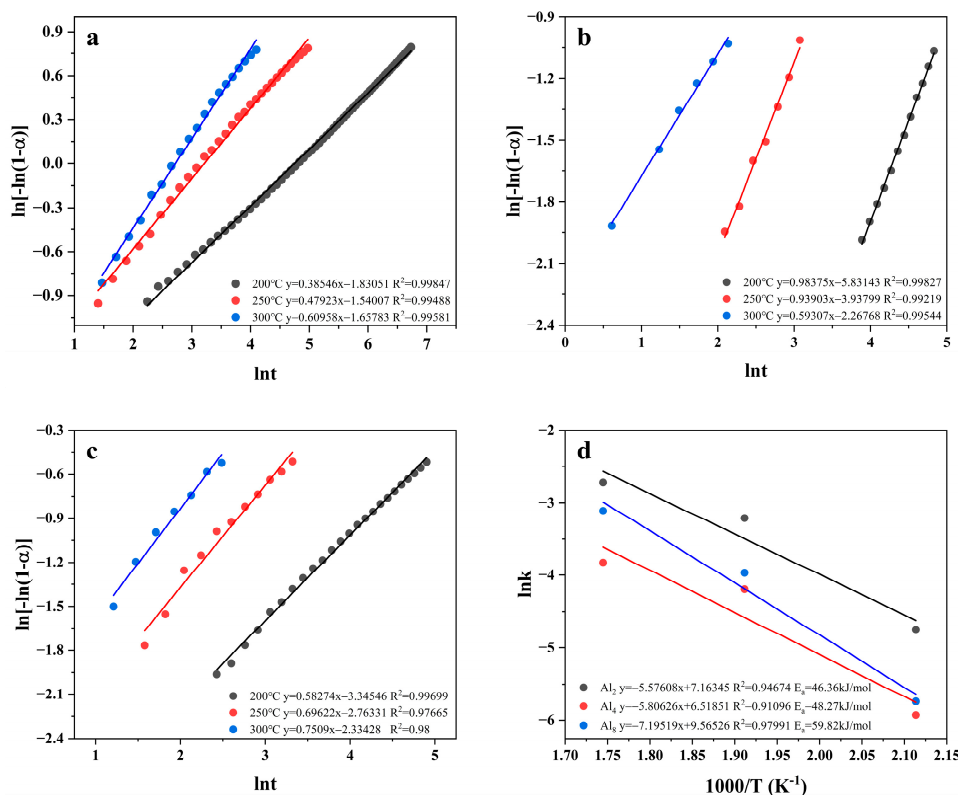


Figure 12. Avrami plots and Arrhenius plots and apparent activation energy of hydrogen absorption E_α of Mg₈₀Ni_{16-x}Al_xY₄ ($x = 2, 4, 8$) alloy: (a) Al₂; (b) Al₄; (c) Al₈; (d) Arrhenius Plots.

3.4. Hydrogen Absorption Thermodynamics and Low-Pressure Hydrogenation Properties

P-C-T curves were measured at 200 °C, 250 °C, and 300 °C to explore the thermodynamics of the three alloys, as shown in Figure 13. The characteristic P-C-T data are summarized in Table 2. Two plateaus existed in the Al₂ and Al₄ alloys, especially at 250 °C and 300 °C. The higher plateau corresponds to the Mg₂Ni phase and the lower one belongs to Mg. The higher plateau of Mg₂Ni of the Al₈ alloy is faint, which is consistent with the microstructure characterization that Mg₂Ni significantly decreased with added Al. Plateaus below 250 °C of all three alloys are lower than 1 bar, indicating close affinity with hydrogen. The Al₄ alloy presents the highest hydrogen absorption ability at all three temperatures, which is consistent with the result of kinetic measurement. In addition, the plateau pressure gradually decreased with increasing Al, indicating an increase in the thermodynamic stability. The hydrogen absorption enthalpies were calculated based on Vant' Hoff equation [17]:

$$\ln\left(\frac{P_H}{P_0}\right) = \frac{\Delta H}{RT} - \frac{\Delta S}{R} \quad (3)$$

P_H is the equilibrium pressure of hydrogen absorption; P_0 is the standard atmospheric pressure; R is the gas constant; T is the absolute temperature, and ΔH and ΔS are changes in the enthalpy and entropy, respectively.

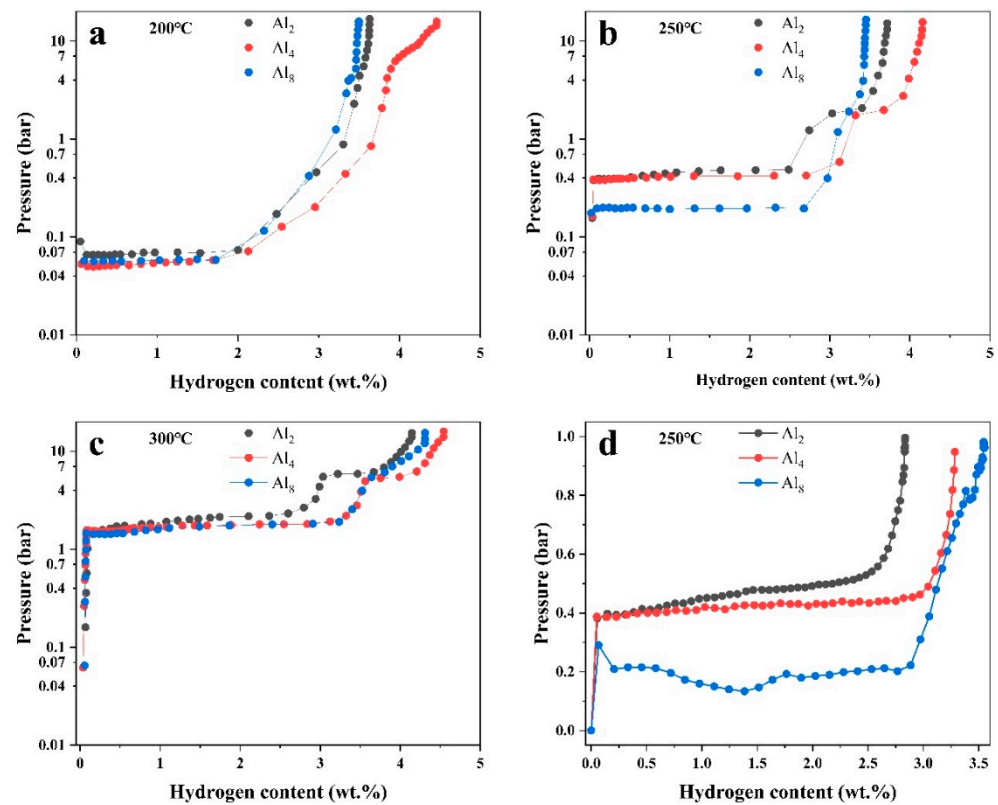


Figure 13. P-C-T curves of (a) Al₂, (b) Al₄, and (c) Al₈ alloys at different temperatures and (d) pressure hydrogen absorption contents under less than 1 bar.

ΔH can be calculated by the slope according to Vant' Hoff equation, as displayed in Figure 14; the corresponding data are listed in Table S4 in the Supplementary Materials. Hydrogen absorption enthalpies of the three alloys were lower than the pure MgH₂ (72.29 kJ/mol as reported by ref. [53]). This trend agrees well with the change in equilibrium pressure of hydrogen absorption of the three alloys, demonstrating the enhancement of thermodynamic stability of the hydrides. Yu et al. reported that the hydrogen absorption enthalpy of the unalloyed Mg₈₀Ni₁₅Y₅ alloy [26] was -62.6 kJ/mol H₂, indicating the decreasing trend by adding Al. This trend agrees well with the change in equilibrium

pressure of hydrogen absorption of the three alloys, demonstrating the enhancement of thermodynamic stability of the hydrides.

Table 2. Characteristic P-C-T data obtained from the corresponding P-C-T curves of the $Mg_{80}Ni_{16-x}Al_xY_4$ ($x = 2, 4, 8$) as-cast alloys.

Samples	Temperature (°C)	H _{ab} (wt.%)	P _{ab} (Bar)
Mg ₈₀ Ni ₁₄ Al ₂ Y ₄	200	3.63	0.07
	250	3.72	0.49
	300	4.14	2.16
Mg ₈₀ Ni ₁₂ Al ₄ Y ₄	200	4.46	0.06
	250	4.16	0.42
	300	4.54	1.92
Mg ₈₀ Ni ₈ Al ₈ Y ₄	200	3.50	0.06
	250	3.45	0.20
	300	4.31	1.90

H_{ab}—absorbed hydrogen. P_{ab}—absorption pressures.

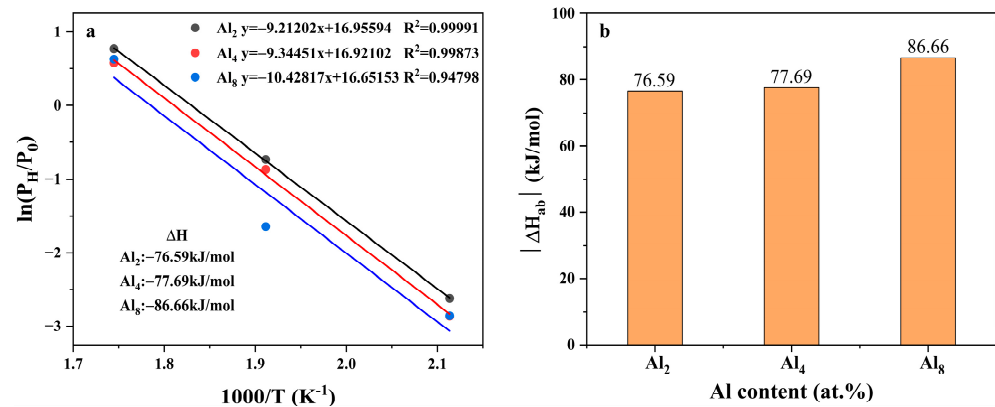


Figure 14. Van't Hoff plots and relationship between the absolute enthalpy of hydrogen absorption of $Mg_{80}Ni_{16-x}Al_xY_4$ ($x = 2, 4, 8$) and Al content: (a) Van't Hoff plots; (b) The relationship between hydrogen absorption enthalpy and Al content.

Theoretically, Al can hardly dissolve into the crystal lattice of Mg; therefore, the increase in thermodynamic stability is considered to not be directly related to the increase in Al. Instead, Y is reported to solid solute into Mg to a certain extent, which is, thus, suggested to be responsible for the change in the plateau pressure. Although the exact mechanism is still confused, speculation is that the solid solution of Y in Mg may be related to the solidification route and Y content. As mentioned above, block Mg rather than strip eutectic was observed in the Al₈ alloy, which illustrated the preferential formation of Mg. Therefore, more Y was likely to dissolve into Mg in the early stage of the solidification process.

For some applications, such as industrial residual of hydrogen, the export hydrogen pressure is quite low, which is the approximate atmosphere. Hydrogen absorption ability at low hydrogen pressure is, thus, considered to be critical to the usability of the Mg-based alloys. To examine the hydrogen absorption ability at low pressure, hydrogen absorption tests were measured by staged p-hydrogenation experiments at 250 °C, where the hydrogen pressure was set at 1 bar for every hydrogen absorption test. The pressure after hydrogenation and the total hydrogen absorption content were recorded, as shown in Figure 13d. The result shows that the Al₈ alloy presents minimum residual pressure at a low pressure of no more than 1 bar. Furthermore, nearly 3.5 wt.% hydrogen can be absorbed in the Al₈ alloy. This is consistent with the thermodynamics assessment, as discussed above, illustrating improved low-pressure hydrogen absorption ability by increasing Al.

3.5. Phase Transformation during Hydrogen Ab/Desorption

XRD patterns of the three alloys after hydrogenation are displayed in Figure 15; the measured profiles were refined based on the Rietveld method. The phase compositions of hydrogenated alloys are listed in Table 3. The hydrogenated $Mg_{80}Ni_{14}Al_2Y_4$ alloy consists of MgH_2 , Mg_2NiH_4 , $Mg_2NiH_{0.29}$, YH_2 , YH_3 , $YMgNi_4$, and $AlNi$. The $Mg_2NiH_{0.29}$ is the intermediate product of Mg_2Ni hydrogenating to Mg_2NiH_4 in the hydrogenation process. The existence of YH_x is attributed to the disproportionation of $Mg_{15}NiY$ upon hydrogenation, which has been reported by Song et al. [24]. The result indicated that $YMgNi_4$ and $AlNi$ did not participate in hydrogenation. As reported, $YMgNi_4$ reacted with hydrogen only under a pressure higher than 4 MPa when the temperature was 80 °C [54], thus retained in the present work due to the low hydrogen pressure.

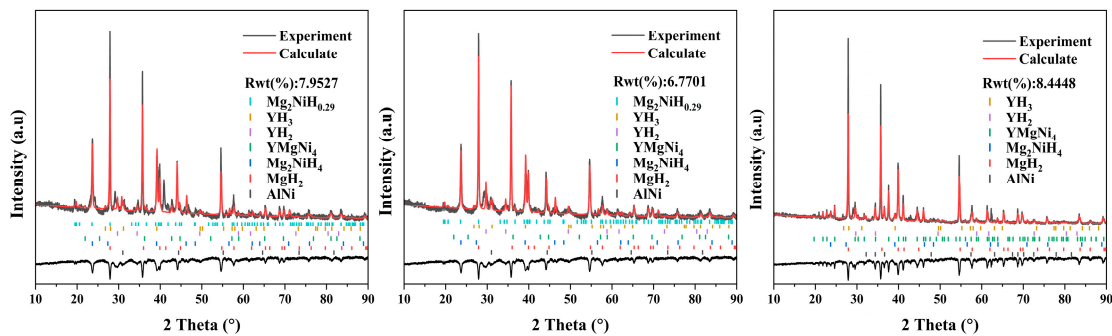


Figure 15. XRD patterns of hydrogenated as-cast $Mg_{80}Ni_{16-x}Al_xY_4$ ($x = 2, 4, 8$) alloys.

Table 3. Contents of phases of $Mg_{80}Ni_{16-x}Al_xY$ ($x = 2, 4, 8$) as-cast alloys after hydrogenation/dehydrogenation.

Phase	Hydrogenated (wt.%)			Dehydrogenated (wt.%)		
	Al2	Al4	Al8	Al2	Al4	Al8
MgH_2	65.26 (± 4.57)	71.41 (± 2.07)	73.32 (± 0.87)	-	-	-
Mg_2NiH_4	16.62 (± 1.17)	13.94 (± 0.38)	1.89 (± 0.10)	-	-	-
$Mg_2NiH_{0.29}$	4.59 (± 0.44)	3.94 (± 0.90)	-	-	-	-
YH_2	1.35 (± 0.0)	2.73 (± 0.61)	1.16 (± 0.05)	1.85 (± 0.08)	3.34 (± 0.01)	1.93 (± 0.07)
YH_3	1.10 (± 0.14)	1.32 (± 0.30)	0.01 (± 0.05)	1.71 (± 0.10)	0.78 (± 0.09)	0.28 (± 0.07)
$AlNi$	9.46 (± 0.69)	6.12 (± 1.40)	-	1.95 (± 0.13)	7.81 (± 0.25)	-
Mg	-	-	5.48 (± 0.20)	51.67 (± 0.01)	65.14 (± 1.72)	75.56 (± 0.0)
Al_3Ni_2Y	-	-	18.14 (± 0.0)	-	-	16.91 (± 0.25)
$YMgNi_4$	1.61 (± 0.21)	0.53 (± 0.01)	-	11.81 (± 0.19)	0.78 (± 0.13)	-
Mg_2Ni	-	-	-	31.02 (± 0.42)	22.16 (± 0.62)	5.61 (± 0.23)

For Al_4 alloy, the phase composition is identical to that of the Al_2 alloy except for a change in content. Due to the rise in Al content and the combination of Al and Ni elements, the Al_4 alloy may have a higher Mg content, which leads to an increase in the hydrogen uptake of the alloy compared to the Al_2 alloy. As the Al content continues to increase, the phase composition of the alloy changes. The hydrogenated Al_8 alloy consists of Mg , MgH_2 , Mg_2NiH_4 , YH_2 , YH_3 , and Al_3Ni_2Y phases. Abundant Al_3Ni_2Y can be detected, indicating nonreaction of Al_3Ni_2Y with hydrogen. In addition, the diffraction peaks of Mg can be observed due to the unfavorable effect of the increased Al content on the hydrogen absorption kinetics, making incomplete hydrogenation of Mg. In general, MgH_2 increases, but Mg_2NiH_4 decreases after hydrogenation. This is consistent with the trend of the phase constitution of the as-cast alloys that shows that adding Al decreases the abundance of Mg_2Ni .

Figure 16 shows the XRD profiles after dehydrogenation. The content of each phase in the alloys after dehydrogenation is also summarized in Table 3.

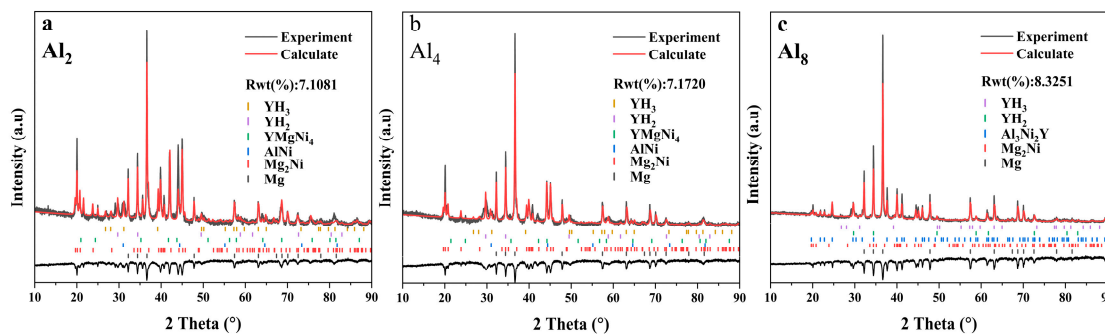


Figure 16. XRD patterns of dehydrogenated as-cast $\text{Mg}_{80}\text{Ni}_{16-x}\text{Al}_x\text{Y}_4$ ($x = 2, 4, 8$) alloys: (a) $\text{Mg}_{80}\text{Ni}_{14}\text{Al}_2\text{Y}_4$; (b) $\text{Mg}_{80}\text{Ni}_{12}\text{Al}_4\text{Y}_4$; (c) $\text{Mg}_{80}\text{Ni}_8\text{Al}_8\text{Y}_4$.

The dehydrogenated Al_2 alloy is composed of Mg, Mg_2Ni , YMgNi_4 , AlNi , YH_2 , and YH_3 . The presence of YH_x indicates that the hydride remains stable at the experimental temperature and has a high thermodynamic stability. The YMgNi_4 phase is also stabilized during the hydrogen absorption/del absorption process, illustrating the negative effect on the hydrogen storage property of YMgNi_4 . The dehydrogenated Al_4 alloy has the same phase structure as the Al_2 alloy, with an increased Mg content and a decreased Mg_2Ni phase, which leads to an increase in the hydrogen uptake of the alloy compared to the Al_2 alloy. The YMgNi_4 phase content decreases substantially due to the increase in Al and the combination of Al and Ni. As to the dehydrogenated Al_8 alloy, more Mg and less Mg_2Ni were illustrated, which corresponded with the phase constitution of the as-cast alloy. Although Al_8 alloy presents the highest Mg content, a large number of residual $\text{Al}_3\text{Ni}_2\text{Y}$ results in low hydrogen absorption content. A decrease in YH_x with an increase in Al resulted from the formation of $\text{Al}_3\text{Ni}_2\text{Y}$, which did not participate in the hydrogenation reaction.

4. Conclusions

1. $\text{Mg}_{80}\text{Ni}_{16-x}\text{Al}_x\text{Y}_4$ ($x = 2, 4, 8$) alloys present multi-phase microstructure, including Mg, Mg_2Ni , YMgNi_4 , AlNi , Mg_{15}NiY , and $\text{Al}_3\text{Ni}_2\text{Y}$. An increase in Al resulted in a decrease in Mg_2Ni and YMgNi_4 due to the reduction in Ni while promoting $\text{Al}_3\text{Ni}_2\text{Y}$;
2. The Al_4 alloy showed fine Mg, Mg_2Ni , and Mg_{15}NiY ternary eutectic. However, grain coarsening was induced by a further increase in Al. Instead of ternary eutectic, the Al_8 alloy revealed binary eutectic and independently solidified Mg caused by alternation of the solidification path;
3. The Al_2 and Al_4 alloys can be hydrogenated at no more than 200 °C. But increase in Al elevated the apparent activation energy and worsened the activation and hydrogen absorption kinetic property;
4. More than 4 wt.% hydrogen can be absorbed by all the alloys at 300 °C. Al reduced the hydrogen absorption enthalpy, leading to an increase in the thermodynamic stability of MgH_2 . Al improved low-pressure hydrogen absorption ability, and 3.5 wt.% hydrogen could be absorbed by Al_4 alloy under only 1 bar hydrogen pressure at 250 °C.

Supplementary Materials: The following supporting information can be downloaded at: <https://www.mdpi.com/article/10.3390/met14010126/s1>, Table S1: Crystal structures of intermetallic compounds in the present study. Table S2: Unit cell parameters of the original alloy. Table S3: Kinetic data points. Table S4: Thermodynamic data points.

Author Contributions: Conceptualization, Y.L., Z.L., G.Z. and F.Y.; formal analysis, X.D., Y.L. and Y.Z.; investigation, X.D., Y.L. and Y.Z.; resources, Z.L., G.Z. and F.Y.; data curation, X.D. and Y.Z.; methodology, Y.L., Z.L., G.Z. and F.Y.; supervision, Y.L., Z.L., G.Z. and F.Y.; writing—original draft, X.D. and Y.L.; writing—review and editing, X.D., Y.L., Y.Z. and Z.L.; funding acquisition, Y.L. All authors have read and agreed to the published version of the manuscript.

Funding: This work is supported by the National Natural Science Foundation of China (51961032 and 51962028), Innovation Foundation of Inner Mongolia University of Science and Technology (2019YQL03), Major Science and Technology Project of Inner Mongolia (2021ZD0029), Program for Young Talents of Science and Technology in Universities of Inner Mongolia Autonomous Region (NJYT23005, NJYT23007), Inner Mongolia Natural Science Foundation (2022LHMS05021), Research Science Project of Colleges and Universities in Inner Mongolia (NJZY21399).

Data Availability Statement: The data presented in this study are available on request from the corresponding author. The data are not publicly available due to ongoing research on this topic.

Conflicts of Interest: The authors declare no conflict of interest.

References

1. Shang, Y.Y.; Pistidda, C.; Gizer, G.; Klassen, T.; Dornheim, M. Mg-based materials for hydrogen storage. *J. Magnes. Alloys* **2021**, *9*, 1837–1860. [[CrossRef](#)]
2. Han, B.; Yu, S.B.; Wang, H.; Lu, Y.S.; Lin, H.J. Nanosize effect on the hydrogen storage properties of Mg-based amorphous alloy. *J. Scr. Mater.* **2022**, *216*, 114736. [[CrossRef](#)]
3. Edalati, K.; Akiba, E.; Botta, W.J.; Estrin, Y.; Floriano, R.; Fruchart, D.; Grosdidier, T.; Horita, Z.; Huot, J.; Li, H.W.; et al. Impact of severe plastic deformation on kinetics and thermodynamics of hydrogen storage in magnesium and its alloys. *J. Mater. Sci.* **2023**, *146*, 221–239. [[CrossRef](#)]
4. Guo, M.C.; Wang, H.; Liu, J.W.; Ouyang, L.Z. Improving hydrogen-induced crystallization and electrochemical hydrogen storage properties of MgNi amorphous alloy with CoB addition. *J. Non-Cryst. Solids* **2022**, *588*, 121646. [[CrossRef](#)]
5. Xu, N.; Yuan, Z.R.; Ma, Z.H.; Guo, X.L.; Zhu, Y.F.; Zou, Y.J.; Zhang, Y. Effects of highly dispersed Ni nanoparticles on the hydrogen storage performance of MgH₂. *Int. J. Miner. Met. Mater.* **2023**, *30*, 54–62. [[CrossRef](#)]
6. Cao, W.C.; Ding, X.; Zhang, Y.; Zhang, J.X.; Chen, R.R.; Su, Y.Q.; Guo, J.J.; Fu, H.Z. Enhanced de-/hydrogenation kinetics of a hyper-eutectic Mg₈₅Ni_{15-x}Ag_x alloy facilitated by Ag dissolving in Mg₂Ni. *J. Alloys Compd.* **2022**, *917*, 165457. [[CrossRef](#)]
7. Li, Z.J.; Zhou, C.S.; Fang, Z.G.Z.; Robert, C.B.J.; Lu, J.; Chai, R. Isothermal hydrogenation kinetics of ball-milled nano-catalyzed magnesium hydride. *Materialia* **2019**, *5*, 100227. [[CrossRef](#)]
8. Imamura, H.; Masanari, K.; Kushara, M.; Katsuoto, H.; Sumi, T.; Sakata, Y. High hydrogen storage capacity of nanosized magnesium synthesized by high energy ball-milling. *J. Alloys Compd.* **2005**, *386*, 211–216. [[CrossRef](#)]
9. Shao, H.; Felderhoff, M.; Schüth, F. Hydrogen storage properties of nanostructured MgH₂/TiH₂ composite prepared by ball milling under high hydrogen pressure. *Int. J. Hydrogen Energy* **2011**, *36*, 10828–10833. [[CrossRef](#)]
10. Li, W.Y.; Li, C.S.; Ma, H.; Chen, J. Magnesium nanowires: Enhanced kinetics for hydrogen absorption and desorption. *J. Am. Chem. Soc.* **2007**, *129*, 6710–6711. [[CrossRef](#)]
11. Sui, Y.Q.; Yuan, Z.M.; Zhou, D.S.; Zhai, T.T.; Li, X.M.; Feng, D.C.; Li, Y.M.; Zhang, Y.H. Recent progress of nanotechnology in enhancing hydrogen storage performance of magnesium-based materials: A review. *Int. J. Hydrogen Energy* **2022**, *47*, 30546–30566. [[CrossRef](#)]
12. Wang, Z.X.; Tian, Z.H.; Yao, P.F.; Zhao, H.M.; Xia, C.Q.; Yang, T. Improved hydrogen storage kinetic properties of magnesium-based materials by adding Ni₂P. *Renew. Energy* **2022**, *189*, 559–569.
13. Lu, Z.Y.; Yu, H.J.; Lu, X.; Song, M.C.; Wu, F.Y.; Zheng, J.G.; Yuan, Z.F.; Zhang, L.T. Two-dimensional vanadium nanosheets as a remarkably effective catalyst for hydrogen storage in MgH₂. *Rare Met.* **2021**, *40*, 3195–3204. [[CrossRef](#)]
14. Jangir, M.; Jain, A.; Yamaguchi, S.; Ichikawa, T.; Lal, C.; Jain, I.P. Catalytic effect of TiF₄ in improving hydrogen storage properties of MgH₂. *Int. J. Hydrogen Energy* **2016**, *41*, 14178–14183. [[CrossRef](#)]
15. Kuamr, S.; Jain, A.; Yamaguchi, S.; Miyaoka, H.; Ichikawa, T.; Mukherjee, A.; Dey, G.K.; Kojima, Y. Surface modification of MgH₂ by ZrCl₄ to tailor the reversible hydrogen storage performance. *Int. J. Hydrogen Energy* **2017**, *42*, 6152–6159. [[CrossRef](#)]
16. Tan, X.F.; Kim, M.; Yasuda, K.; Nogita, K. Strategies to enhance hydrogen storage performances in bulk Mg-based hydrides. *J. Mater. Sci. Technol.* **2023**, *153*, 139–158. [[CrossRef](#)]
17. Yang, X.L.; Lu, X.H.; Zhang, J.Q.; Hou, Q.H.; Zou, J.H. Progress in improving hydrogen storage properties of Mg-based materials. *Mater. Today Adv.* **2023**, *19*, 100387.
18. Darriet, B.; Pezat, M.; Hbika, A.; Hagenmuller, P. Application of magnesium rich rare-earth alloys to hydrogen storage. *Int. J. Hydrogen Energy* **1980**, *5*, 173–178. [[CrossRef](#)]
19. Hanada, N.; Ichikawa, T.; Fujii, H. Catalytic effect of nanoparticle 3d-transition metals on hydrogen storage properties in magnesium hydride MgH₂ prepared by mechanical milling. *J. Phys. Chem. B* **2005**, *109*, 7188–7194. [[CrossRef](#)]
20. Yong, H.; Wang, S.; Ma, J.W.; Zhang, K.W.; Zhao, D.L.; Hu, J.F.; Zhang, Y.H. Dual-tuning of de-/hydrogenation kinetic properties of Mg-based hydrogen storage alloy by building a Ni-/Co-multi-platform collaborative system. *Int. J. Hydrogen Energy* **2021**, *46*, 24202–24213. [[CrossRef](#)]
21. Yong, H.; Wei, X.; Wang, Y.H.; Guo, S.H.; Yuan, Z.M.; Qi, Y.; Zhao, D.L.; Zhang, Y.H. Phase evolution, thermodynamics and kinetics property of transition metal (TM = Zr, Ti, V) catalyzed Mg-Ce-Y-Ni hydrogen storage alloys. *J. Phys. Chem. Solids* **2020**, *144*, 109516. [[CrossRef](#)]

22. Xie, L.S.; Li, J.S.; Zhang, T.B.; Kou, H.C. De/hydrogenation kinetics against air exposure and microstructure evolution during hydrogen absorption/desorption of Mg-Ni-Ce alloys. *Renew. Energy* **2017**, *113*, 1399–1407. [[CrossRef](#)]
23. Li, Y.; Gu, Q.F.; Li, Q.; Zhang, T.F. In-situ synchrotron X-ray diffraction investigation on hydrogen-induced decomposition of long period stacking ordered structure in Mg-Ni-Y system. *Scr. Mater.* **2017**, *127*, 102–107. [[CrossRef](#)]
24. Song, W.J.; Dong, H.P.; Zhang, G.; Liu, J.; Yang, G.; Liu, Y.H.; Li, Y.Z.; Li, J.S.; Shen, J.H.; Chen, Y.X.; et al. Enhanced hydrogen absorption kinetics by introducing fine eutectic and long-period stacking ordered structure in ternary eutectic Mg-Ni-Y alloy. *J. Alloys Compd.* **2020**, *820*, 153187. [[CrossRef](#)]
25. Kang, H.L.; Yong, H.; Wang, J.Z.; Xu, S.X.; Li, L.J.; Wang, S.; Hu, J.F.; Zhang, Y.H. Characterization on the kinetics and thermodynamics of Mg-based hydrogen storage alloy by the multiple alloying of Ce, Ni and Y elements. *Mater. Charact.* **2021**, *182*, 111583. [[CrossRef](#)]
26. Yu, Y.C.; Ji, S.Q.; Zhang, S.H.; Wang, S.; Chen, Y.W.; Yong, H.; Liu, B.S.; Zhang, Y.H. Microstructure characteristics, hydrogen storage thermodynamic and kinetic properties of Mg-Ni-Y based hydrogen storage alloys. *Int. J. Hydrogen Energy* **2022**, *47*, 27059–27070. [[CrossRef](#)]
27. Zhou, S.C.; Pan, R.K.; Luo, T.P.; Wu, D.H.; Wei, L.T.; Tang, B.Y. Ab initio study of effects of Al and Y co-doping on destabilizing of MgH₂. *Int. J. Hydrogen Energy* **2014**, *39*, 9254–9261. [[CrossRef](#)]
28. Tang, R.; Liu, Y.Q.; Zhu, C.C.; Zhu, J.W.; Yu, G. Effect of Al substitution for Co on the hydrogen storage characteristics of Ml_{0.8}Mg_{0.2}Ni_{3.2}Co_{0.6-x}Al_x (x = 0–0.6) alloys. *Intermetallics* **2006**, *14*, 361–366. [[CrossRef](#)]
29. Yang, T.; Zhai, T.T.; Yuan, Z.M.; Bu, W.G.; Xu, S.; Zhang, Y.H. Hydrogen storage properties of LaMgNi_{3.6}M_{0.4} (M = Ni, Co, Mn, Cu, Al) alloys. *J. Alloys Compd.* **2014**, *617*, 29–33. [[CrossRef](#)]
30. Sun, X.Z.; Pan, H.G.; Gao, M.X.; Li, R.; Lin, Y.; Ma, S. Cycling stability of La-Mg-Ni-Co type hydride electrode with Al. *Trans. Nonferrous Met. Soc. China* **2006**, *16*, s834–s838. [[CrossRef](#)]
31. Ershova, O.G.; Dobrovolyak, V.D.; Solonin, Y.M.; Khyzhun, O.Y.; Koval, A.Y. The effect of Al on thermal stability and kinetics of decomposition of MgH₂ prepared by mechanochemical reaction at different conditions. *Mater. Chem. Phys.* **2015**, *162*, 408–416. [[CrossRef](#)]
32. Kan, H.; Zhang, N.; Wang, H. Al-Mg Alloy powders for hydrogen storage. *Adv. Chem. Eng.* **2012**, *550–553*, 497–501. [[CrossRef](#)]
33. Li, S.J.; Yang, L.L.; Zhu, Y.F.; Liu, Y.; Zhang, J.G.; Li, L.Q. Mechanism of improving hydrogenation of Mg by in-situ formation of Al* in hydriding combustion synthesis. *J. Alloys Compd.* **2022**, *911*, 164969. [[CrossRef](#)]
34. Lan, Z.Q.; Peng, W.Q.; Wei, W.L.; Xu, L.Q.; Guo, J. Preparation and hydrogen storage properties of Mg-Al-Li solid solution. *Int. J. Hydrogen Energy* **2016**, *41*, 6134–6138. [[CrossRef](#)]
35. Liu, T.; Qin, C.G.; Zhu, M.; Cao, Y.R.; Shen, H.L.; Li, X.G. Synthesis and hydrogen storage properties of Mg-La-Al nanoparticles. *J. Power Sources* **2012**, *219*, 100–105. [[CrossRef](#)]
36. Crivello, J.-C.; Nobuki, T.; Kato, S.; Abe, M.; Kuji, T. Hydrogen absorption properties of the γ -Mg₁₇Al₁₂ phase and its Al-richer domain. *J. Alloys Compd.* **2007**, *446–447*, 157–161. [[CrossRef](#)]
37. Lu, W.C.; Ou, S.F.; Lin, M.H.; Wong, M.F. Hydrogen absorption/desorption performance of Mg-Al alloys synthesized by reactive mechanical milling and hydrogen pulverization. *J. Alloys Compd.* **2016**, *682*, 318–325. [[CrossRef](#)]
38. Zhong, H.C.; Wang, H.; Ouyang, L.Z. Improving the hydrogen storage properties of MgH₂ by reversibly forming Mg-Al solid solution alloys. *Int. J. Hydrogen Energy* **2014**, *39*, 3320–3326. [[CrossRef](#)]
39. Cao, W.C.; Ding, X.; Zhang, Y.; Zhang, J.X.; Chen, R.R.; Su, Y.Q.; Guo, J.J.; Fu, H.Z. Formation of AlNi phase and its influence on hydrogen absorption kinetics of Mg₇₇Ni_{23-x}Al_x alloys at intermediate temperatures. *Int. J. Hydrogen Energy* **2022**, *47*, 25733–25744. [[CrossRef](#)]
40. Ren, L.; Li, Y.H.; Lin, X.; Ding, W.J.; Zou, J.X. Promoting hydrogen industry with high-capacity Mg-based solid-state hydrogen storage materials and systems. *Front. Energy* **2023**, *17*, 320–323. [[CrossRef](#)]
41. Wang, H.G.; Liu, Y.F.; Zhang, J. Hydrogen purification by Mg alloy hydrogen adsorbent. *Adsorption* **2022**, *28*, 85–95. [[CrossRef](#)]
42. Saville, A.I.; Creuziger, A.; Mitchell, E.B.; Vogel, S.C.; Benzing, J.T.; Klemm-Toole, J.; Clarke, K.D.; Clarke, A.J. MAUD Rietveld Refinement Software for Neutron Diffraction Texture Studies of Single and Dual-Phase Materials. *Integr. Mater. Manuf. Innov.* **2021**, *10*, 36936346. [[CrossRef](#)] [[PubMed](#)]
43. Sheppard, D.A.; Paskevicius, M.; Javadian, P.; Davies, I.J.; Buckley, C.E. Methods for accurate high-temperature Sieverts-type hydrogen measurements of metal hydrides. *J. Alloys Compd.* **2019**, *787*, 1225–1237. [[CrossRef](#)]
44. Zhu, Y.M.; Morton, A.J.; Nie, J.F. The 18R and 14H long-period stacking ordered structures in Mg-Y-Zn alloys. *Acta Mater.* **2010**, *58*, 2936–2947. [[CrossRef](#)]
45. Asadi, A.H.; Kalayeh, P.M.; Mirzadeh, H.; Malekan, M.; Emamy, M. Precipitation kinetics and mechanical properties of Mg-Y-Zn and Mg-Y-Ni alloys containing long-period stacking ordered (LPSO) structures. *J. Mater. Res. Technol.* **2023**, *24*, 9513–9522. [[CrossRef](#)]
46. Jiang, M.; Zhang, S.; Bi, Y.D.; Li, Y.P.; Qin, G.W. Phase equilibria of the long-period stacking ordered phase in the Mg-Ni-Y system. *Intermetallics* **2015**, *57*, 127–132. [[CrossRef](#)]
47. Lu, R.P.; Jiao, K.; Li, N.T.; Hou, H.; Wang, J.F.; Zhao, Y.H. Microstructure and damping properties of LPSO phase dominant Mg-Ni-Y and Mg-Zn-Ni-Y alloys. *J. Alloys Compd.* **2022**, 250543791. [[CrossRef](#)]
48. Song, W.J.; Ma, W.H.; He, S.; Chen, W.; Shen, J.H.; Sun, D.L.; Wei, Q.M.; Yu, X.B. TiO₂@C catalyzed hydrogen storage performance of Mg-Ni-Y alloy with LPSO and ternary eutectic structure. *J. Alloys Compd.* **2023**, 258666888. [[CrossRef](#)]

49. Friedrichs, O.; Sánchez-López, J.C.; López-Cartes, C.; Dornheim, M.; Klassen, T.; Bormann, R.; Fernández, A. Chemical and microstructural study of the oxygen passivation behaviour of nanocrystalline Mg and MgH₂. *Appl. Surf. Sci.* **2006**, *252*, 2334–2345. [[CrossRef](#)]
50. Avrami, M. Kinetics of Phase Change. I General Theory. *J. Chem. Phys.* **1939**, *7*, 1103–1112. [[CrossRef](#)]
51. Xu, E.; You, X.M.; Bu, C.; Zhang, L.F.; Wang, Q.; Zhao, Z.G. Influence of micro-amount O₂ or N₂ on the hydrogenation/dehydrogenation kinetics of hydrogen-storage material MgH₂. *Int. J. Hydrogen Energy* **2017**, *42*, 8057–8062. [[CrossRef](#)]
52. Hou, Q.H.; Zhang, J.Q.; Guo, X.T.; Xu, G.Z.; Yang, X.L. Synthesis of low-cost biomass charcoal-based Ni nanocatalyst and evaluation of their kinetic enhancement of MgH₂. *Int. J. Hydrogen Energy* **2022**, *47*, 15209–15223. [[CrossRef](#)]
53. Dong, J.J.; Panda, S.; Zhu, W.; Zou, J.X.; Ding, W.J. Enhanced hydrogen sorption properties of MgH₂ when doped with mechanically alloyed amorphous Zr_{0.67}Ni_{0.33} particles. *Int. J. Hydrogen Energy* **2020**, *45*, 28144–28153. [[CrossRef](#)]
54. Aono, K.; Orimo, S.; Fujii, H. Structural and hydriding properties of MgYNi₄:: A new intermetallic compound with C15b-type Laves phase structure. *J. Alloys Compd.* **2000**, *309*, L1–L4. [[CrossRef](#)]

Disclaimer/Publisher’s Note: The statements, opinions and data contained in all publications are solely those of the individual author(s) and contributor(s) and not of MDPI and/or the editor(s). MDPI and/or the editor(s) disclaim responsibility for any injury to people or property resulting from any ideas, methods, instructions or products referred to in the content.